Small

NANO · MICRO small
www.small-journal.com

RESEARCH ARTICLE

Structured Selective Activation for Bubble-Controlled High-Rate Alkaline OER

Youngseob Lee[1] | Donggeun Eom[2] | Sangwook Park[2,3,4,5] | Hyoungsoon Lee[1,6]

[1]Department of Intelligent Energy and Industry, Chung-Ang University, Seoul, South Korea | [2]Department of Mechanical Engineering, Seoul National University, Seoul, South Korea | [3]Institute of Advanced Machines and Design, Seoul National University, Seoul, South Korea | [4]Institute of Engineering Research, Seoul National University, Seoul, South Korea | [5]Seoul National University Energy Initiative, Seoul National University, Seoul, South Korea | [6]Department of Mechanical Engineering, Chung-Ang University, Seoul, South Korea

Correspondence: Sangwook Park (swparkk@snu.ac.kr) | Hyoungsoon Lee (leeh@cau.ac.kr)

Received: 26 December 2025 | **Accepted:** 27 January 2026

Keywords: amorphous catalyst | gas bubble dynamics | mass transport | oxygen evolution reaction | selective activation

ABSTRACT

Efficient gas bubble management is critical for advancing alkaline oxygen evolution electrodes, but scalable and cost-effective designs remain limited. Here we present an asymmetrically activated nickel-plate (NP) electrode that couples selective catalyst activation and structured geometry to guide bubble evolution and enhance mass transport. The electrode is fabricated through micromilling, polytetrafluoroethylene (PTFE) coating, and electrodeposition of amorphous nickel-iron (NiFe) catalysts, forming deactivated and activated regions that promote directional bubble release and electrolyte renewal through gridded microchannels. This asymmetric configuration mitigates transport overpotential at high current densities, achieving 408 mV at 1000 mA cm^{-2} and a high electrochemically active surface area (ECSA)-normalized current density of 210 mA cm^{-2}. The monolithic framework, defect-rich amorphous catalysts, and stable PTFE coating ensure sustained performance for over 100 h. This work demonstrates a simple and scalable structural strategy to control interfacial bubble dynamics, providing both high activity and long-term durability for alkaline oxygen evolution reaction.

1 | Introduction

Water electrolysis has emerged as a pivotal technology for hydrogen production, offering a clean pathway toward decarbonization [1, 2]. It consists of two half-reactions: hydrogen evolution reaction (HER) at the cathode and oxygen evolution reaction (OER) at the anode. While HER proceeds with relatively fast kinetics, OER remains the primary performance bottleneck due to its inherently sluggish four-electron transfer mechanism and high activation energy barriers [3]. This leads to substantial overpotential requirements, limiting the energy efficiency of electrolysis systems [4]. To address these challenges, extensive efforts have been dedicated to developing electrocatalysts with enhanced catalytic activity and durability. Abundant yet efficient non-precious transition metals have become key candidates to meet these demands [5], prompting intensive research into optimizing their oxidation states [6], elemental compositions [7, 8], and structural architectures [9]. However, the intrinsic trade-off between activity and stability of electrocatalysts necessitates alternative approaches to further improve electrochemical performance [10, 11].

Gas bubble nucleation represents a major challenge in electrochemical systems, with water electrolysis being particularly

Youngseob Lee and Donggeun Eom contributed equally to this work.

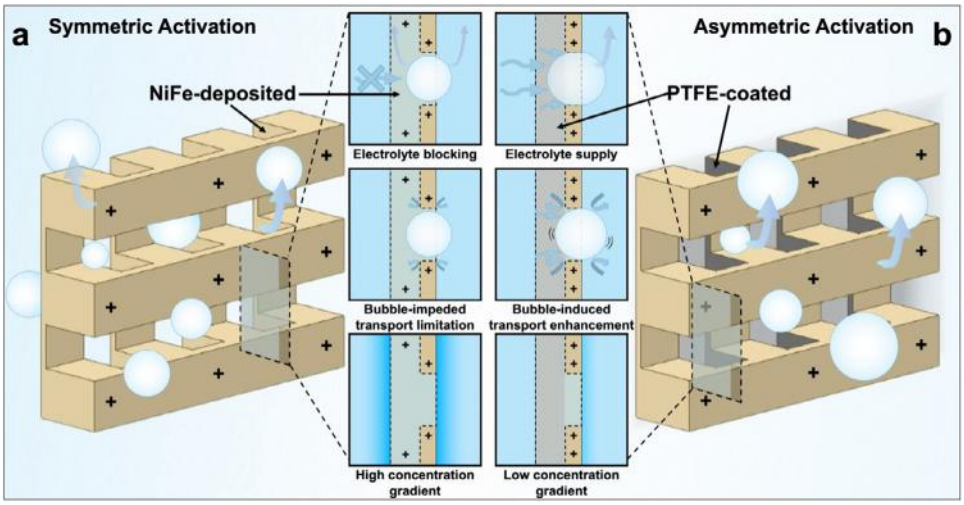

FIGURE 1 | Schematics of electrodes and gas bubble dynamics with three effects on electrochemical performance: electrolyte supply, bubble transport, and concentration boundary layer. (a) Conventionally activated electrode, and (b) asymmetrically activated electrode illustrating mitigated bubble effects on the transport overpotentials.

susceptible to this phenomenon [12–14]. During OER, once gas molecular clusters exceed the critical radius, they grow and accumulate on the electrode surface, blocking active sites and impeding ion and mass transport until detachment occurs [15, 16]. The effect becomes especially pronounced at high current densities, as rapid oxygen generation accelerates bubble growth and worsens mass transport. Bubble accumulation contributes to activation, concentration, and ohmic overpotentials by reducing the electrochemically active surface area (ECSA), thickening the diffusion boundary layer, and adding gas-phase resistance [17]. To mitigate these effects, superaerophobic (superhydrophilic) electrode surfaces have been developed to facilitate bubble detachment by lowering adhesion forces, often through micro-/nanostructural modifications [11, 18–25]. Such designs effectively shorten bubble residence time and enable buoyancy-driven release at smaller bubble sizes [26]. In parallel, compositional tuning of catalysts through surface oxidation to form hydroxides or oxides [27], chemical functionalization with tailored groups [28, 29], and heteroatom doping [30, 31] have been explored to adjust surface energy and wettability, thereby influencing bubble nucleation behavior. More recently, bio-inspired and heterogeneous-wettability electrodes have been proposed to spatially separate bubble nucleation and release sites or to maintain aerophilic cushions driven by Laplace pressure, enabling bubble-free gas evolution at high current densities [32–36]. Despite their effectiveness, these strategies rely on intricate structures and complex fabrication, limiting scalability for practical applications.

From the perspective of interfacial dynamics, it remains challenging for catalysts on structured electrodes to fully and efficiently contribute to electrochemical reactions [37, 38]. In many cases, increasing the ECSA does not guarantee intrinsic gains and can even depress apparent activity under suboptimal mass transport [39, 40]. This discrepancy intensifies at high current densities (Figure 1a), as bubble growth and delayed departure exacerbate transport overpotential [17]. Meanwhile, the reliance on intricate architectures and sophisticated catalyst syntheses raises concerns over scalability and industrial deployment. To address these limitations, bubble-driven electrode architectures with electrically deactivated regions have the potential to leverage interfacial dynamics and regulate local mass transport and concentration gradients, thereby improving efficiency (Figure 1b) [41, 42].

Herein, we demonstrate a scalable approach for fabricating nickel plate (NP) electrodes that enhance mass transport via asymmetric activation and bubble transport [43]. The approach uses micromilling, polytetrafluoroethylene (PTFE) spray coating, and electrodeposition of amorphous nickel-iron (NiFe) catalysts to create alternating conductive and electrically insulated regions that form electrolyte and ion pathways. Unlike prior PTFE-based studies that harnessed wettability to control nucleation rate [44–46], we exploit PTFE's low electrical conductivity to deactivate catalytic activity and drive Laplace-induced microconvection without membranes or external forces. Amorphous NiFe hydroxide with partially insulated surfaces reduces dependence on surface wettability [41, 47, 48], and maintains tolerance to structural degradation under intensive gas evolution [49, 50–53]. Consequently, the engineered electrode delivers 1000 mA cm^{-2} at an overpotential of 408 mV and sustains stable operation for over 100 hours [54, 55]. These outcomes are achieved without high ECSA substrates or complex nanostructuring, establishing an architecture-driven, scalable design principle.

2 | Results and Discussion

An asymmetric anode was fabricated through several steps, including mechanical micromilling, PTFE coating, and electrodeposition of an amorphous NiFe catalyst. Figure 2a outlines the entire fabrication sequence of the DC / NiFe-R electrode, in which DC and NiFe-R refer to the deactivated column and NiFe-deposited row, respectively. First, a columnar microchannel pattern was produced on one side of the NP substrate using a TiAlN-coated micro flat endmill (300 μm width). To render this surface electrically inactive, a silica-based PTFE suspension was sprayed four times and cured at 135°C for 24 h, forming a reliable insulating layer. Subsequently, a row-type microchannel array was machined on the opposite side with the same milling

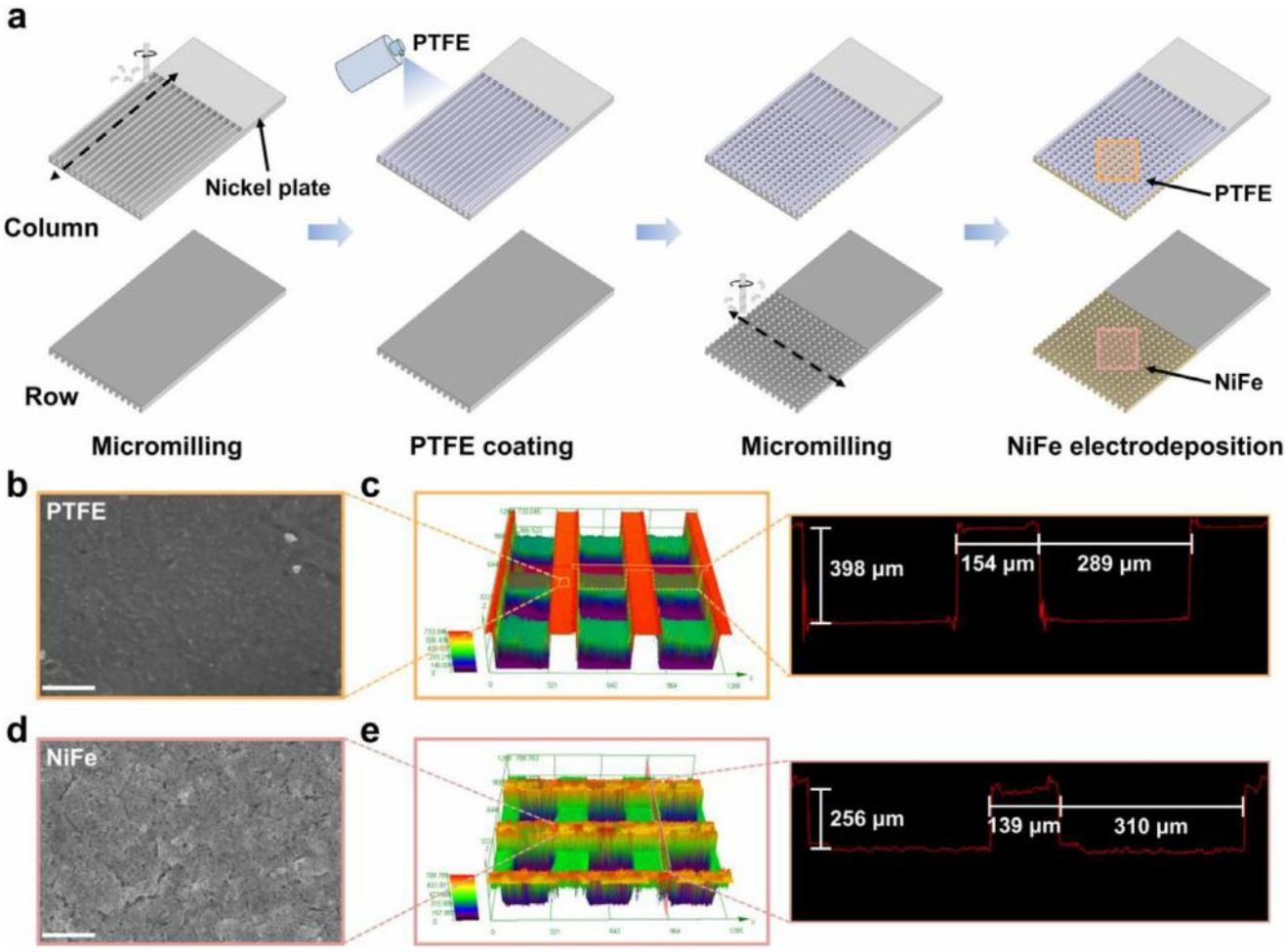

FIGURE 2 | Schematic fabrication processes of DC / NiFe-R (representative case) and its structural visualization. (a) Manufacturing procedure and electrode schematics. (b) SEM image of PTFE-coated deactivated surfaces (column) and (c) its confocal image with geometrical dimensions. (d) SEM image of amorphous NiFe-deposited activated surfaces (row) and (e) its confocal image with geometrical dimensions. Scale bars are 1 μm.

TABLE 1 | Experimental test matrix of anodes.

Samples	One side	Another side	Structural features
NP	Ni		Symmetric structure
NiFe-NP	NiFe		Symmetric structure
NiFe-NP / NiFe-R	NiFe	NiFe Row	Asymmetric structure
NiFe-C / NiFe-R	NiFe Column	NiFe Row	Asymmetric structure
DC / NiFe-R	PTFE Column	NiFe Row	Asymmetric structure and activation

parameters, followed by electrodeposition of the NiFe catalyst to selectively activate the PTFE-free regions. Because PTFE possesses extremely low electrical conductivity ($\chi \sim 10^{-24} - 10^{-20}$ S/m) [42], the coated areas remained completely inert throughout electrodeposition and OER tests, prohibiting both catalyst formation and electrochemical activity (Figures S1 and S2). In contrast, the uncoated row microchannels retained metallic conductivity, serving as the active pathways for OER.

Several asymmetric electrode variants were prepared, and their configurations are summarized in Table 1. Among them, NiFe-NP, NiFe-NP / NiFe-R, and NiFe-C / NiFe-R all contained NiFe catalysts on both sides but differed in geometric configuration (Figure S3). Scanning electron microscopy (SEM) images revealed distinct nanostructural contrasts between NiFe-deposited and PTFE-coated regions (Figure 2b,d). X-ray diffraction (XRD) patterns exhibited no peak near 23.5°, confirming the amorphous nature of the NiFe catalyst and the absence of crystallinity typically associated with layered double hydroxides (Figure S4) [8]. Instead, the spectra showed sharp substrate peaks and broad intensity fluctuations attributed to amorphous NiFe domains. X-ray photoelectron spectroscopy (XPS) identified Ni and Fe mainly in the Ni^{2+} and Fe^{3+} oxidation states (Figure S5) [47, 56]. Energy-dispersive spectroscopy (EDS) further confirmed

compositional heterogeneity, detecting enriched fluorine content on the deactivated PTFE regions (Figure S6). Consistent with the low electrical conductivity of PTFE, EDS counts from these areas were significantly lower than those of the conductive surfaces.

Confocal microscopy revealed the geometric dimensions of the column and row microchannels (Figure 2c,e). Because the same 300 μm endmill was used for all micromachining steps, both channels shared identical widths (~300 μm). The columns exhibited a depth of ~400 μm and wall thickness of ~150 μm, whereas the rows showed a depth of ~250 μm and wall thickness of ~150 μm. These dimensions were optimized to minimize undesired bubble pinning during OER and applied uniformly to all electrode types listed in Table 1. Considering the 500 μm thickness of the NP substrate, the intersecting column and row channels form a 3D gridded network that facilitates electrolyte and ion transport (Figure S7). Detailed fabrication procedures are provided in the Methods section.

Even with identical substrate geometries, the asymmetrically activated electrode exhibited markedly different gas-bubble dynamics from the symmetrically activated one. Figure 3a–d compares NiFe-C / NiFe-R and DC / NiFe-R electrodes, together with schematic representations recorded at 1000 mA cm^{-2} (normalized by geometric projection area; Video S1). In NiFe-C / NiFe-R, amorphous NiFe catalysts covered the entire surface, so all regions actively participated in the OER. During operation, vigorous bubble growth and detachment occurred at both column and row surfaces, as clearly visible from the side view (Figure 3a). Although the gridded microchannel framework provided mass-transport pathways, bubble accumulation still obstructed ion and electrolyte flow, increasing transport overpotential (Figures 1a and 3b).

In contrast, DC / NiFe-R displayed distinctive bubble behavior originating from asymmetric activation. While not enforcing perfectly unidirectional gas release as in state-of-the-art designs [32, 33], the electrode showed pronounced differences between the deactivated column and the activated row surfaces. These contrasts are directly visible in Figure 3c and Video S1, demonstrating that OER did not occur on the PTFE-coated columns owing to their extremely low conductivity (Figure S2). Bubbles occasionally observed on the deactivated columns resulted from reverse migration through the gridded microchannels, primarily driven by local wettability gradients (Note S1). Consequently, the openings through the deactivated columns acted as electrolyte and ion transport channels, reducing bubble accumulation on the column side and promoting efficient, directional bubble release from the opposing row surfaces (Figure 3d).

Visualization of DC / NiFe-R clarifies the mechanism responsible for lowering transport overpotential at high current densities (Figure 1b). Figure $3e_1$–e_3 highlights three dominant bubble dynamics phenomena observed at the activated rows of DC / NiFe-R at 1000 mA cm^{-2} (Video S2). The first is microconvection (Figure $3e_1$), occurring as bubbles detach and alleviate local O_2 concentration gradients [13]. Gas nucleation primarily took place within the row microchannels, where bubbles merged and intermittently clogged before being expelled outward by curvature-driven pressure (Laplace pressure), producing localized convective flow. These flows disrupted the concentration boundary layer and agitated neighboring bubbles without direct contact, facilitating their detachment. For example, bubble departure within a row channel generated oscillatory electrolyte motion that triggered sequential release of adjacent bubbles. The second dynamic is bubble-bubble collision (Figure $3e_2$), which arises when large velocity disparities exist among bubbles [57]. A clogged bubble detaching at high speed collided with nearby smaller bubbles without coalescence, as the short contact time prevented film rupture, forcing smaller bubbles to detach whose buoyancy alone was insufficient. The third is coalescence (Figure $3e_3$), observed when slower interactions allow bubbles to merge [58]. A buoyant bubble rising at terminal velocity outside the row microchannel coalesced with a clogged bubble, converting surface energy into kinetic energy and propelling the combined bubble away from the electrode. This release of surface energy explains the strong oscillatory motion captured during coalescence (Video S2).

All these phenomena intensify with increasing bubble size [59]. From nucleation to merging, clogging, and detachment, these processes predominantly occur within the row microchannels of DC / NiFe-R, producing larger bubbles and consequently stronger bubble-induced flows. Here, "merging" denotes the accumulation of bubbles within the row microchannels, while "coalescence" refers to their external joining after detachment. Bubble departure diameters measured at the activated regions confirm this trend (Figure $3f_1$,f_2). Since DC / NiFe-R has lower ECSA compared to symmetrically activated electrodes, higher current density becomes concentrated on its smaller area. Consequently, the reaction rate intensifies, and bubble dynamics occur more actively. While reactions that occur simultaneously on both sides of symmetrically activated electrodes are now localized to one side, this concentrated reaction activity results in more intensive bubble generation and larger bubble sizes. Given the 300 μm channel width, the distributions in Figure $3f_2$ and Video S1 reveal more frequent clogging of larger bubbles in DC / NiFe-R than in NiFe-C / NiFe-R. Unlike conventional electrodes that rely on buoyancy force for bubble detachment, DC / NiFe-R harnesses Laplace pressure as the driving force, where the increased bubble departure diameter enhances local flow intensity without compromising performance, as the deactivated columns continuously supply electrolyte and ions. This interplay between selective activation and geometry-driven flow effectively mitigates transport overpotential under high current densities [60]. Further discussion, including a sub-optimal asymmetric case illustrating interfacial dynamics and wettability effects, is provided in Note S1 and Figure S8 [17].

Linear sweep voltammetry (LSV) was performed to assess the OER activity of the electrodes in 1.0 M KOH using a standard three-electrode configuration. Figure 4a presents the LSV curves of all electrodes listed in Table 1, comparing the performance of DC / NiFe-R with the other designs. The current density j was normalized to the projected electrode area. The pristine NP exhibited the largest overpotential, reaching 370 mV at 10 mA cm^{-2} (η_{10}), whereas the NiFe-based electrodes showed η_{10} values below 300 mV, confirming that the amorphous NiFe catalyst markedly enhanced OER activity. As the current density increased to 1000 mA cm^{-2}, performance differences among the electrodes became more distinct, reflecting the influence of geometric and activation effects.

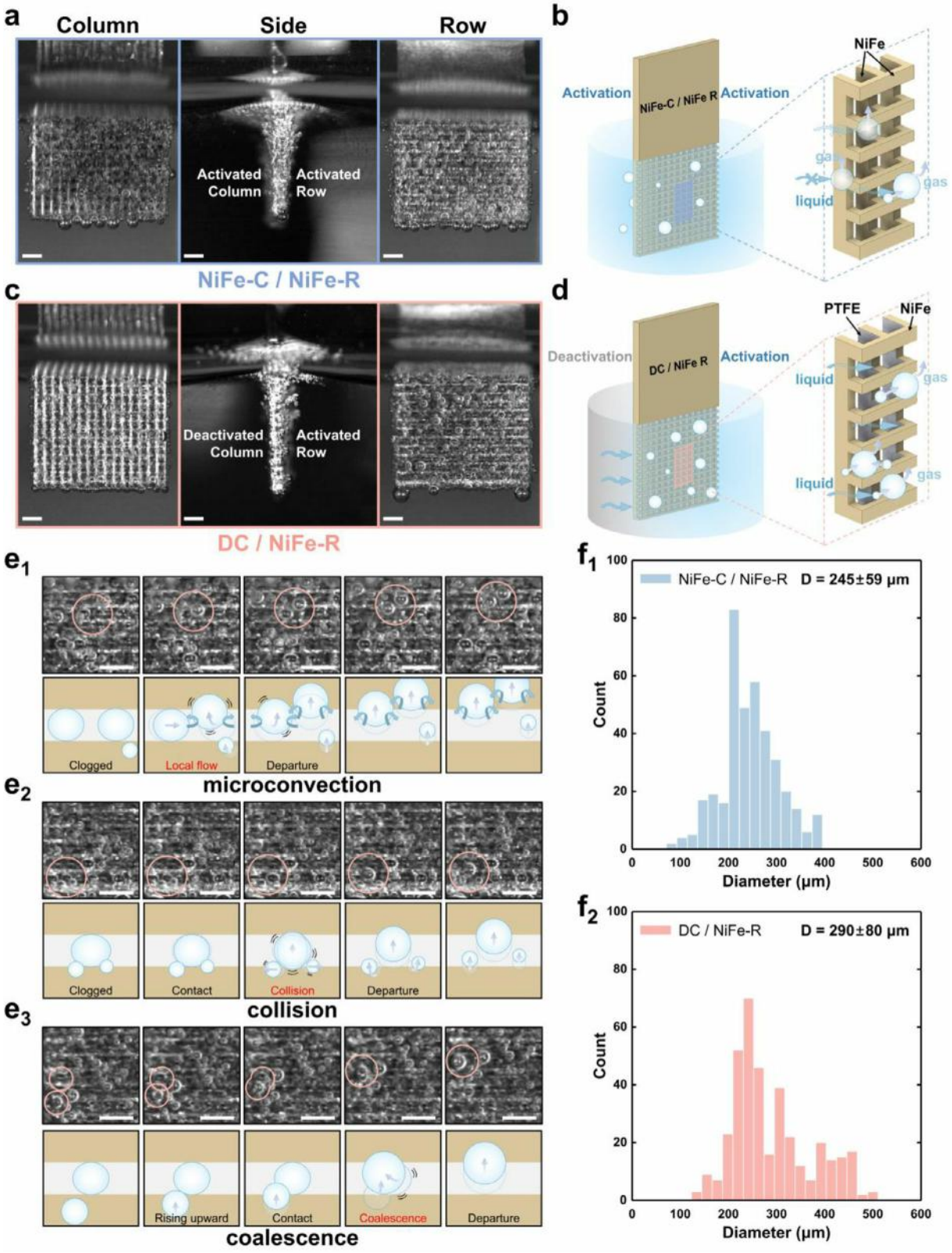

FIGURE 3 | High-speed bubble dynamics captured at 4000 frames per second, with corresponding schematics and bubble departure diameters. (a) Visualization of NiFe-C / NiFe-R: column surface, side view, and row surface (from left to right), and (b) its schematic illustration of the bubble dynamics. (c) Visualization of DC / NiFe-R: deactivated column surface, side view, and row surface (from left to right), and (d) its schematic illustration of the bubble dynamics. (e_1–e_3) Detailed views of three representative bubble dynamics–microconvection, collision, and coalescence–with corresponding schematics. Each image was extracted at 20 frames (5 ms) intervals. (f_1,f_2) Bubble departure diameters measured at 1000 mA cm^{-2} from NiFe-C / NiFe-R and DC / NiFe-R, respectively (immobile bubbles excluded). Error values represent standard deviations. Scale bars are 1 mm.

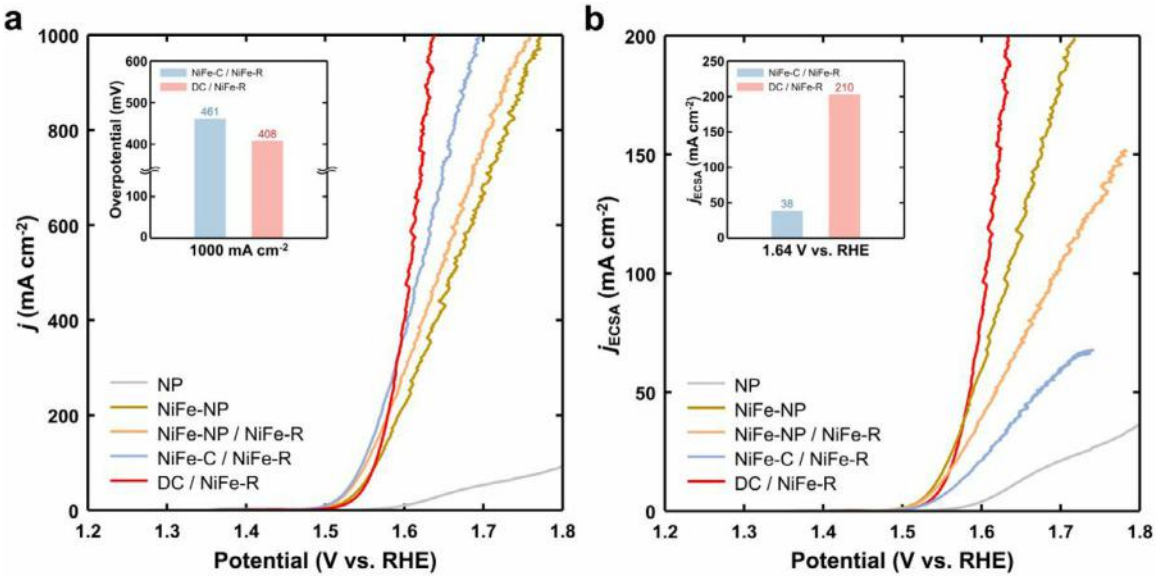

FIGURE 4 | Electrochemical OER performance of the electrodes. (a) LSV polarization curves, where j denotes a current density normalized by geometric projection area (7 mm × 7 mm; inset: overpotential of NiFe-C / NiFe-R and DC / NiFe-R at 1000 mA cm^{-2}). (b) LSV polarization curves, where j_{ECSA} denotes a current density normalized by ECSA (inset: j_{ECSA} of NiFe-C / NiFe-R and DC / NiFe-R at 1.64 V vs. RHE).

At low current densities, a clear correlation was observed between electrochemically active surface area (ECSA) and overpotential (Figures S9 and S10). Additional micromilling from NiFe-NP to NiFe-C / NiFe-R increased the number of microchannels and the physical surface area, enlarging the ECSA from 1.83 to 8.52 cm^2 and lowering η_{10} from 286 to 271 mV. In contrast, the partially PTFE-coated DC / NiFe-R possessed a smaller ECSA of 2.42 cm^2 and a slightly higher η_{10} of 293 mV. The dependence on ECSA was further verified through electrochemical impedance spectroscopy (EIS). The charge-transfer resistance (R_{ct}) of NiFe-C / NiFe-R was lower than that of DC / NiFe-R, consistent with their relative ECSAs (1.53 V vs. RHE; Figure S11). At high current densities approaching 1,000 mA cm^{-2}, however, transport limitations became the dominant performance bottleneck [42, 61], reversing the trend observed under kinetic-controlled conditions. DC / NiFe-R achieved the lowest overpotential of 408 mV at 1000 mA cm^{-2}, substantially outperforming NiFe-C / NiFe-R (461 mV). The symmetrically activated electrodes maintained the typical trend of decreasing overpotential with increasing ECSA at lower current densities.

The superior OER performance of DC / NiFe-R cannot be explained solely by surface area effects. As shown in Figure 4b, when the current density was normalized by ECSA (j_{ECSA}), NiFe-C / NiFe-R displayed a higher overpotential, indicating that increased ECSA alone did not guarantee improved performance owing to inefficient mass transport [39]. Despite its lower geometric ECSA, DC / NiFe-R exhibited a comparably high j_{ECSA} (Figure S12). With increasing overpotential, j_{ECSA} of DC / NiFe-R rose more sharply, reaching 210 mA cm^{-2} at 410 mV. Such enhancement signifies effective gas-bubble regulation and efficient electrolyte and ion transport through coordinated bubble dynamics within the gridded microchannels and deactivated regions. This inverse correlation with ECSA highlights that DC / NiFe-R outperformed all other electrodes under conditions dominated by vigorous gas evolution, underscoring the central role of structural asymmetry and transport optimization at high current densities.

To more comprehensively assess OER performance with respect to mass transport, the Tafel slopes of the electrodes were compared, as shown in Figure 5a. For consistent and reliable fitting, the linear region was selected from the portion of the Tafel plot exhibiting a constant slope, together with high R^2 values from linear regression (Figure S13) [62, 63]. All NiFe-deposited electrodes exhibited lower Tafel slopes than the pristine NP electrode, confirming their enhanced catalytic kinetics. Among them, DC / NiFe-R showed a slightly higher Tafel slope of 41.0 mV dec^{-1}. Because the fitting range was primarily below 1.55 V vs. RHE, this value reflects the influence of ECSA previously discussed in Figure 4a.

To examine diffusion limitations and mass-transport effects, the linear range of the Tafel slopes was quantified and plotted alongside other performance metrics in Figure 5b [47, 64, 65]. The Tafel slope of DC / NiFe-R retained linearity for 1.8 decades, suggesting that transport-induced constraints were effectively mitigated by the deactivated regions. For additional performance metrics governed by gas-bubble behavior, such as η_{1000}, j at 400 mV overpotential, and j_{ECSA} at 400 mV overpotential, DC / NiFe-R consistently outperformed NiFe-C / NiFe-R, reinforcing the advantage of asymmetric activation in sustaining efficient mass transport under gas-evolving conditions.

Long-term stability was further evaluated by chronopotentiometry (CP) at 1,000 mA cm^{-2}, where the y-axis represents iR-compensated cell voltage (Figure 5c). Because mechanical and electrochemical degradation can accelerate under vigorous gas nucleation, particularly at high current densities [37], the test was conducted at 25°C with continuous temperature control. Periodic voltage drops, appearing approximately every 24 h, corresponded to electrolyte replenishment. The cell voltage remained stable

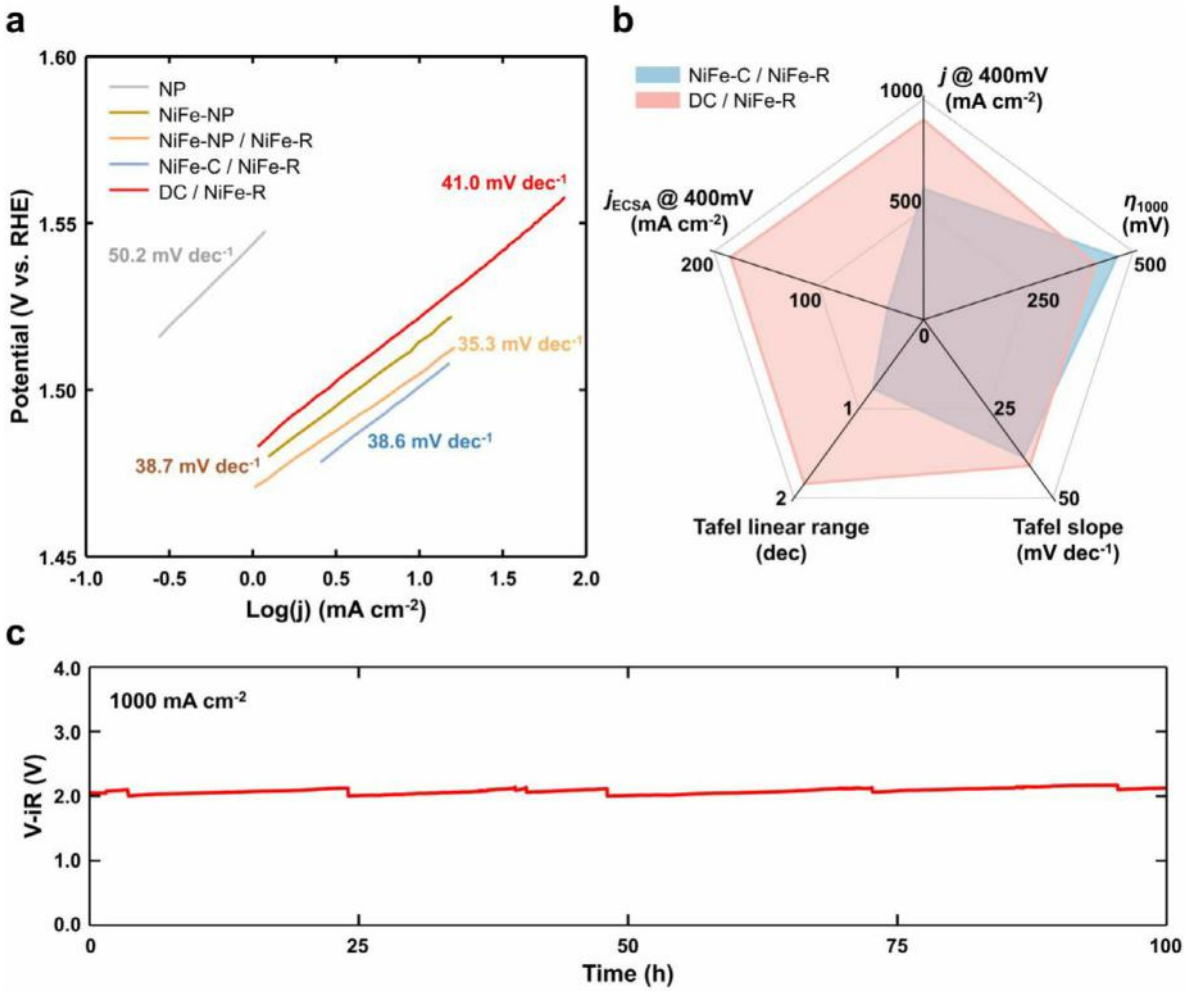

FIGURE 5 | Comprehensive electrochemical performance and long-term stability of the electrodes. (a) Linear Tafel slopes of the electrodes. (b) Comparison of OER performance metrics between NiFe-C / NiFe-R and DC / NiFe-R. (c) CP measurement confirming the long-term stability of DC / NiFe-R at 1000 mA cm^{-2}.

over 100 h of continuous operation, confirming the durability of DC / NiFe-R. Post-OER characterization further supported this result: SEM images revealed no noticeable morphological deterioration of the NiFe catalyst (Figure S14), while the ECSA slightly increased due to self-reconstruction of the amorphous NiFe, which is defect-rich and capable of forming new active sites [25, 66–69]. The integrated NP substrate, chemically stable PTFE coating in strong alkaline media, and amorphous NiFe catalysts together ensured excellent long-term durability of the DC / NiFe-R electrode (Figures S15 and S16).

3 | Conclusion

We established a scalable and cost-effective electrode framework that effectively overcomes bubble-induced transport limitations in alkaline oxygen evolution. Through micromilling, PTFE coating, and electrodeposition of amorphous NiFe catalysts, the DC / NiFe-R architecture achieved asymmetric activation and the formation of robust electrolyte and ion transport pathways. Interfacial dynamics governed the overall mass transport process, where large-bubble interactions, including microconvection, collision, and coalescence, promoted rapid bubble release and sustained electrolyte renewal under high current densities. The defect-rich amorphous NiFe underwent self-reconstruction, increasing the electrochemically active surface area while maintaining morphological integrity. As a result, the electrode delivered high activity at industrially relevant current densities (η_{1000} = 408 mV) and maintained stable operation for 100 h at 1000 mA cm^{-2}. This study establishes a versatile structural design paradigm that complements catalytic optimization, offering a scalable route toward durable, high-performance electrodes for practical alkaline water electrolysis.

4 | Methods

4.1 | Preparation of Nickel Plate Anode

In all experiments, nickel plates (NP; Ni 99.9 wt.%, 7 mm × 7 mm, 0.5 mm thickness) were used as the anode substrates. Micromilling was first performed on one side of the NP using a TiAlN-coated micro flat endmill (300 μm width) to create microchannel structures, oriented either horizontally (R; row) or vertically (C; column). The samples were then sonicated in 3 M HCl solution for 10 min to remove oxides, rinsed with ethanol

and deionized water (18.2 MΩ·cm resistivity), and then dried with nitrogen gas to ensure the quality of subsequent steps, including polytetrafluoroethylene (PTFE) coating and secondary micromilling. To fabricate asymmetric electrodes with electrically deactivated regions, the micromilled surface was spray-coated with PTFE four times, solidified, and cured at 135°C for 24 h. The opposite side of the electrode was then processed with the same milling method but a different orientation to create orthogonally interconnected microchannels. For instance, if columns (C) were coated with PTFE on one side, rows (R) were milled on the opposite side. After all micromilling steps, the electrodes were thoroughly cleaned by sonicating in isopropyl alcohol and deionized water, followed by drying at room temperature. Prior to catalyst synthesis, the electrodes were electrochemically pre-conditioned by five cycles of cyclic voltammetry (CV) in the potential range of 0.0–0.8 V vs. a mercury/mercuric oxide (Hg|HgO) at a scan rate of 50 mV s^{-1} in 1 M KOH [8]. Amorphous nickel-iron (NiFe) catalysts were then electrodeposited, where the NP substrate, a Pt mesh, and a saturated calomel electrode (SCE) were employed as a working electrode, counter electrode, and reference electrode, respectively. A constant potential of -0.9 V vs. SCE was applied for 15 min in 3 mM $Ni(NO_3)_2{\cdot}6H_2O$ + 3 mM $Fe(NO_3)_3{\cdot}9H_2O$ electrolyte at 25°C. After electrodeposition, the working electrodes were gently rinsed with deionized water and dried with nitrogen gas.

4.2 | Characterization

Structural morphology of electrodes and catalysts was characterized by field-emission SEM (Carl Zeiss, SIGMA 360) at 5 kV accelerating voltage. 3D images and geometrical dimensions of the structured electrodes were obtained using confocal microscopy (Olympus, OLS4100). Crystalline structures were analyzed by XRD (Bruker-AXS, New D8-Advance) with Cu Kα radiation (λ = 1.5418 Å) at a scan speed of 1° min^{-1}. Elemental compositions were characterized by XPS (ThermoFisher, Scientific K-alpha+) and EDS. Gas bubble dynamics were recorded using a high-speed camera (Photron, FASTCAM Mini UX100) at 4000 frames per second. Bubble departure diameters were measured from the captured footage using ImageJ software. To ensure only detached mobile bubbles were analyzed, images separated by 20 frames (5 ms) were compared and processed in MATLAB R2023b with the Image Processing Toolbox and Computer Vision Toolbox, thereby excluding clogged immobile bubbles from the quantitative analysis (Figure S15).

4.3 | Electrochemical Measurements

All electrochemical measurements were carried out in 1 M KOH at 25°C electrolyte using a BioLogic SP-300 potentiostat. Before OER testing, the electrolyte was purged with nitrogen gas for 15 min to remove dissolved gases. A three-electrode system was employed, where an NP-based electrode, a Pt mesh, and a Hg|HgO were used as a working electrode, a counter electrode, and a reference electrode, respectively. CV scanning was first conducted in a non-faradaic region (−0.05 to 0.05 V vs. open circuit voltage) at different scan rates of 50, 100, 150, 200, 250, and 300 mV s^{-1}. The double-layer capacitance (C_{dl}) was calculated from the slope of current densities vs. scan rates. Electrochemical surface area (ECSA) was estimated from C_{dl} and the specific capacitance (C_s; 40 μF cm^{-2}). The detailed calculation process is specified in Note S2. Electrochemical impedance spectroscopy (EIS) was carried out at 1.53 V vs. RHE with a sinusoidal amplitude of 10 mV across a frequency range from 100 kHz to 100 mHz. The solution resistance obtained from Nyquist plots was used for 95% iR-compensation. Unless otherwise stated, all reported potentials were compensated by 95% iR-compensation. Linear sweep voltammetry (LSV) was performed at a scan rate of 5 mV s^{-1}. Measured potentials vs. Hg|HgO were converted to the potentials vs. RHE by the Nernst equation: $E_{RHE} = E_{Hg/HgO} + 0.059\times pH + 0.105$ V, where pH is 13.89 and 0.105 V represents the standard potential of Hg/HgO under 1 M KOH [70, 71]. Long-term OER stability was evaluated through chronopotentiometry (CP), with the results reported as raw cell voltages.

Acknowledgements

This work was supported by the National Research Foundation of Korea (NRF) grant funded by the Korea government (MSIT) (No. RS-2024-00411577, No. RS-2024-00353227, and No. RS-2023-00213633).

Conflicts of Interest

The authors declare no conflicts of interest.

Data Availability Statement

The data that support the findings of this study are available from the corresponding author upon reasonable request.

References

1. O. J. Guerra, J. Eichman, J. Kurtz, and B.-M. Hodge, "Cost Competitiveness of Electrolytic Hydrogen," *Joule* 3 (2019): 2425–2443.

2. S. Chu and A. Majumdar, "Opportunities and Challenges for a Sustainable Energy Future," *Nature* 488 (2012): 294–303.

3. X. Xie, L. Du, L. Yan, et al., "Oxygen Evolution Reaction in Alkaline Environment: Material Challenges and Solutions," *Advanced Functional Materials* 32 (2022): 2110036.

4. N.-T. Suen, S.-F. Hung, Q. Quan, N. Zhang, Y.-J. Xu, and H. M. Chen, "Electrocatalysis for the Oxygen Evolution Reaction: Recent Development and Future Perspectives," *Chemical Society Reviews* 46 (2017): 337–365.

5. J. Zhao, J. Zhang, Z. Li, and X. Bu, "Recent Progress on NiFe-Based Electrocatalysts for the Oxygen Evolution Reaction," *Small* 16 (2020): 2003916.

6. F. Dionigi, Z. Zeng, I. Sinev, et al., "In-Situ Structure and Catalytic Mechanism of NiFe and CoFe Layered Double Hydroxides during Oxygen Evolution," *Nature Communications* 11 (2020): 2522.

7. C. C. L. McCrory, S. Jung, J. C. Peters, and T. F. Jaramillo, "Benchmarking Heterogeneous Electrocatalysts for the Oxygen Evolution Reaction," *Journal of the American Chemical Society* 135 (2013): 16977–16987.

8. L. Trotochaud, S. L. Young, J. K. Ranney, and S. W. Boettcher, "Nickel–Iron Oxyhydroxide Oxygen-Evolution Electrocatalysts: The Role of Intentional and Incidental Iron Incorporation," *Journal of the American Chemical Society* 136 (2014): 6744–6753.

9. H. Song, S. Oh, H. Yoon, K.-H. Kim, S. Ryu, and J. Oh, "Bifunctional NiFe Inverse Opal Electrocatalysts with Heterojunction Si Solar Cells for 9.54%-Efficient Unassisted Solar Water Splitting," *Nano Energy* 42 (2017): 1–7.

10. S. Chen, Z. Niu, C. Xie, et al., "Effects of Catalyst Processing on the Activity and Stability of Pt–Ni Nanoframe Electrocatalysts," *ACS Nano* 12 (2018): 8697–8705.

11. M. Bae, Y. Kang, D. W. Lee, D. Jeon, and J. Ryu, "Superaerophobic Polyethyleneimine Hydrogels for Improving Electrochemical Hydrogen Production by Promoting Bubble Detachment," *Advanced Energy Materials* 12 (2022): 2201452.

12. H. J. Cho, D. J. Preston, Y. Zhu, and E. N. Wang, "Nanoengineered Materials for Liquid–vapour Phase-Change Heat Transfer," *Nature Reviews Materials* 2 (2016): 16092.

13. A. Angulo, P. van der Linde, H. Gardeniers, M. Modestino, and D. F. Rivas, "Influence of Bubbles on the Energy Conversion Efficiency of Electrochemical Reactors," *Joule* 4 (2020): 555–579.

14. D. Qiu, B. Li, C. Zhao, et al., "A Review on Zinc Electrodes in Alkaline Electrolyte: Current Challenges and Optimization Strategies," *Energy Storage Materials* 61 (2023): 102903.

15. P. A. Kempler, R. H. Coridan, and L. Luo, "Gas Evolution in Water Electrolysis," *Chemical Reviews* 124 (2024): 10964–11007.

16. I. J. Ford, "Nucleation Theorems, the Statistical Mechanics of Molecular Clusters, and a Revision of Classical Nucleation Theory," *Physical Review E* 56 (1997): 5615.

17. R. Iwata, L. Zhang, K. L. Wilke, et al., "Bubble Growth and Departure Modes on Wettable/Non-Wettable Porous Foams in Alkaline Water Splitting," *Joule* 5 (2021): 887–900.

18. Z. Lu, W. Zhu, X. Yu, et al., "Ultrahigh Hydrogen Evolution Performance of under-Water "Superaerophobic" MoS_2 Nanostructured Electrodes," *Advanced Materials* 26 (2014): 2683–2687.

19. M. S. Faber, R. Dziedzic, M. A. Lukowski, and N. S. Kaiser, Q. Ding, and S. Jin, "High-Performance Electrocatalysis Using Metallic Cobalt Pyrite (CoS_2) Micro- and Nanostructures," *Journal of the American Chemical Society* 136 (2014): 10053–10061.

20. J. Ma, M. Yang, G. Zhao, et al., "Ni Electrodes with 3D-Ordered Surface Structures for Boosting Bubble Releasing toward High Current Density Alkaline Water Splitting," *Ultrasonics Sonochemistry* 96 (2023): 106398.

21. J. Kim, S.-M. Jung, N. Lee, K.-S. Kim, Y.-T. Kim, and J. K. Kim, "Efficient Alkaline Hydrogen Evolution Reaction Using Superaerophobic Ni Nanoarrays with Accelerated H_2 Bubble Release," *Advanced Materials* 35 (2023): 2305844.

22. Q. Ren, L. Feng, C. Ye, et al., "Nanocone-Modified Surface Facilitates Gas Bubble Detachment for High-Rate Alkaline Water Splitting," *Advanced Energy Materials* 13 (2023): 2302073.

23. Y. Li, H. Zhang, T. Xu, et al., "Under-Water Superaerophobic Pine-Shaped Pt Nanoarray Electrode for Ultrahigh-Performance Hydrogen Evolution," *Advanced Functional Materials* 25 (2015): 1737–1744.

24. X. Yu, Z.-Y. Yu, X.-L. Zhang, et al., ""Superaerophobic" Nickel Phosphide Nanoarray Catalyst for Efficient Hydrogen Evolution at Ultrahigh Current Densities," *Journal of the American Chemical Society* 141 (2019): 7537–7543.

25. X. Shan, J. Liu, H. Mu, et al., "An Engineered Superhydrophilic/Superaerophobic Electrocatalyst Composed of the Supported CoMoS X Chalcogel for Overall Water Splitting," *Angewandte Chemie International Edition* 59 (2020): 1659–1665.

26. M. Li, P. Xie, L. Yu, L. Luo, and X. Sun, "Bubble Engineering on Micro-/Nanostructured Electrodes for Water Splitting," *ACS Nano* 17 (2023): 23299–23316.

27. Z. Yan, H. Sun, X. Chen, et al., "Anion Insertion Enhanced Electrodeposition of Robust Metal Hydroxide/Oxide Electrodes for Oxygen Evolution," *Nature Communications* 9 (2018): 2373.

28. Y. Li and C. Zhao, "Enhancing Water Oxidation Catalysis on a Synergistic Phosphorylated NiFe Hydroxide by Adjusting Catalyst Wettability," *ACS Catalysis* 7 (2017): 2535–2541.

29. X. Yuan, T. Yan, Z. Liu, and P. Kang, "Highly Efficient Alkaline Water Electrolysis Using Alkanolamine-Functionalized Zirconia-Blended Separators," *ACS Sustainable Chemistry & Engineering* 11 (2023): 4269–4278.

30. N. Han, K. R. Yang, Z. Lu, et al., "Nitrogen-Doped Tungsten Carbide Nanoarray as an Efficient Bifunctional Electrocatalyst for Water Splitting in Acid," *Nature Communications* 9 (2018): 924.

31. Q. Li, F. Huang, S. Li, H. Zhang, and X.-Y. Yu, "Oxygen Vacancy Engineering Synergistic with Surface Hydrophilicity Modification of Hollow Ru Doped CoNi-LDH Nanotube Arrays for Boosting Hydrogen Evolution," *Small* 18 (2022): 2104323.

32. J. Li, Y. Zhu, W. Chen, et al., "Breathing-Mimicking Electrocatalysis for Oxygen Evolution and Reduction," *Joule* 3 (2019): 557–569.

33. K. Deng, H. Feng, Y. Zhang, D. Liu, and Q. Li, "Ampere-Level Membrane-Less Water Electrolysis Enabled by Rose-Petal-Effect-Mimetic Interface," *Joule* 7 (2023): 1852–1866.

34. C. Zhang, Z. Xu, N. Han, et al., "Superaerophilic/Superaerophobic Cooperative Electrode for Efficient Hydrogen Evolution Reaction via Enhanced Mass Transfer," *Science Advances* 9 (2023): add6978.

35. C. Zhang, C. Teng, S. Guo, et al., "Superaerophilic/Superaerophobic NiFe-LDHs Electrode for Enhancing Overall Water Splitting in Alkaline Media," *Nano Letters* 24 (2024): 1959–1966.

36. Z. Long, Y. Zhao, C. Zhang, et al., "A Multi-Bioinspired Dual-Gradient Electrode for Microbubble Manipulation toward Controllable Water Splitting," *Advanced Materials* 32 (2020): 1908099.

37. K. Zeng and D. Zhang, "Recent Progress in Alkaline Water Electrolysis for Hydrogen Production and Applications," *Progress in Energy and Combustion Science* 36 (2010): 307–326.

38. J. R. Lake, Á. M. Soto, and K. K. Varanasi, "Impact of Bubbles on Electrochemically Active Surface Area of Microtextured Gas-Evolving Electrodes," *Langmuir* 38 (2022): 3276–3283.

39. R. Wu, Z. Hu, H. Zhang, J. Wang, C. Qin, and Y. Zhou, "Bubbles in Porous Electrodes for Alkaline Water Electrolysis," *Langmuir* 40 (2024): 721–733.

40. S. S. Jeon, P. W. Kang, M. Klingenhof, H. Lee, F. Dionigi, and P. Strasser, "Active Surface Area and Intrinsic Catalytic Oxygen Evolution Reactivity of NiFe LDH at Reactive Electrode Potentials Using Capacitances," *ACS Catalysis* 13 (2023): 1186–1196.

41. M. M. Rahman, J. Pollack, and M. McCarthy, "Increasing Boiling Heat Transfer Using Low Conductivity Materials," *Scientific Reports* 5 (2015): 13145.

42. L. Zhang, R. Iwata, Z. Lu, X. Wang, C. D. Díaz-Marín, and Y. Zhong, "Bridging Innovations of Phase Change Heat Transfer to Electrochemical Gas Evolution Reactions," *Chemical Reviews* 124 (2024): 10052–10111.

43. R. D. L. Smith, M. S. Prévot, R. D. Fagan, et al., "Photochemical Route for Accessing Amorphous Metal Oxide Materials for Water Oxidation Catalysis," *Science* 340 (2013): 60–63.

44. O. Teschke and F. Galembeck, "Effect of PTFE Coverage on the Performance of Gas Evolving Electrodes," *Journal of The Electrochemical Society* 131 (1984): 1095.

45. M. U. Kleinke, M. A. B. De Moraes, and O. Teschke, "A New Type of PTFE-Covered Gas Evolving Electrode," *Journal of The Electrochemical Society* 133 (1986): 1815.

46. C. Brussieux, P. H. Viers, H. Roustan, and M. Rakib, "Controlled Electrochemical Gas Bubble Release from Electrodes Entirely and Partially Covered with Hydrophobic Materials," *Electrochimica Acta* 56 (2011): 7194–7201.

47. X. Lu and C. Zhao, "Electrodeposition of Hierarchically Structured Three-Dimensional Nickel–Iron Electrodes for Efficient Oxygen Evolution at High Current Densities," *Nature Communications* 6 (2015): 6616.

48. L. Li, Q. Shao, and X. Huang, "Amorphous Oxide Nanostructures for Advanced Electrocatalysis," *Chemistry – A European Journal* 26 (2020): 3943–3960.

49. Y. Yang, J. Li, W. Yang, et al., "An Open-Structured Carbon fiber Brush Electrode for Efficient Hydrogen Evolution by Inducing Oriented Bubble Transport," *Chemical Engineering Journal* 407 (2021): 127159.

50. L. Wu, Q. Wang, S. Yuan, et al., "Unrevealing the Interaction between Electrode Degradation and Bubble Behaviors in an Anion Exchange Membrane Water Electrolyzer," *Advanced Science* 12 (2025): 2412962.

51. Y. Luo, Y. Wu, D. Wu, et al., "NiFe-Layered Double Hydroxide Synchronously Activated by Heterojunctions and Vacancies for the Oxygen Evolution Reaction," *ACS Applied Materials & Interfaces* 12 (2020): 42850–42858.

52. A. Farmani, F. Fahimi, and F. Nasirpouri, "Relationship between Degradation Mechanism and Water Electrolysis Efficiency of Electrodeposited Nickel Electrodes," *npj Materials Degradation* 9 (2025): 25.

53. D. Li, A. R. Motz, C. Bae, et al., "Durability of Anion Exchange Membrane Water Electrolyzers," *Energy & Environmental Science* 14 (2021): 3393–3419.

54. C. G. Morales-Guio, L.-A. Stern, and X. Hu, "Nanostructured Hydrotreating Catalysts for Electrochemical Hydrogen Evolution," *Chemical Society Reviews* 43 (2014): 6555–6569.

55. Y. Chen, G. Yu, W. Chen, et al., "Highly Active, Nonprecious Electrocatalyst Comprising Borophene Subunits for the Hydrogen Evolution Reaction," *Journal of the American Chemical Society* 139 (2017): 12370–12373.

56. C. Liang, P. Zou, A. Nairan, et al., "Exceptional Performance of Hierarchical Ni–Fe Oxyhydroxide@NiFe Alloy Nanowire Array Electrocatalysts for Large Current Density Water Splitting," *Energy & Environmental Science* 13 (2020): 86–95.

57. S. Orvalho, P. Stanovsky, and M. C. Ruzicka, "Bubble Coalescence in Electrolytes: Effect of Bubble Approach Velocity," *Chemical Engineering Journal* 406 (2021): 125926.

58. R. Iwata, L. Zhang, Z. Lu, S. Gong, J. Du, and E. N. Wang, "How Coalescing Bubbles Depart from a Wall," *Langmuir* 38 (2022): 4371–4377.

59. H. Vogt and K. Stephan, "Local Microprocesses at Gas-Evolving Electrodes and Their Influence on Mass Transfer," *Electrochimica Acta* 155 (2015): 348–356.

60. T. Wu, B. Liu, H. Hao, et al., "Coalescence-Induced Late Departure of Bubbles Improves Water Electrolysis Efficiency," *eScience* (2025): 100472.

61. X. Cheng, Z. Du, Y. Ding, F. Li, Z. Hua, and H. Liu, "Bubble Management for Electrolytic Water Splitting by Surface Engineering: A Review," *Langmuir* 39 (2023): 16994–17008.

62. O. Van Der Heijden, S. Park, J. J. J. Eggebeen, and M. T. M. Koper, "Non-Kinetic Effects Convolute Activity and Tafel Analysis for the Alkaline Oxygen Evolution Reaction on NiFeOOH Electrocatalysts," *Angewandte Chemie International Edition* 62 (2023): 202216477.

63. O. Van Der Heijden, S. Park, R. E. Vos, J. J. J. Eggebeen, and M. T. M. Koper, "Tafel Slope Plot as a Tool to Analyze Electrocatalytic Reactions," *ACS Energy Letters* 9 (2024): 1871–1879.

64. A. B. Laursen, K. R. Patraju, M. J. Whitaker, et al., "Nanocrystalline Ni_5P_4: A Hydrogen Evolution Electrocatalyst of Exceptional Efficiency in both Alkaline and Acidic media," *Energy & Environmental Science* 8 (2015): 1027–1034.

65. Q. Zhang, N. M. Bedford, J. Pan, X. Lu, and R. Amal, "A Fully Reversible Water Electrolyzer Cell Made up from FeCoNi (Oxy)Hydroxide Atomic Layers," *Advanced Energy Materials* 9 (2019): 1901312.

66. H. Han, K. M. Kim, H. Choi, et al., "Parallelized Reaction Pathway and Stronger Internal Band Bending by Partial Oxidation of Metal Sulfide–Graphene Composites: Important Factors of Synergistic Oxygen Evolution Reaction Enhancement," *ACS Catalysis* 8 (2018): 4091–4102.

67. J. Liu and L. Guo, "In Situ Self-Reconstruction Inducing Amorphous Species: A Key to Electrocatalysis," *Matter* 4 (2021): 2850–2873.

68. W. Cai, R. Chen, H. Yang, et al., "Amorphous versus Crystalline in Water Oxidation Catalysis: A Case Study of NiFe Alloy," *Nano Letters* 20 (2020): 4278–4285.

69. Y. Li, G. Zhang, W. Lu, and F. Cao, "Amorphous Ni–Fe–Mo Suboxides Coupled with Ni Network as Porous Nanoplate Array on Nickel Foam: A Highly Efficient and Durable Bifunctional Electrode for Overall Water Splitting," *Advanced Science* 7 (2020): 1902034.

70. K. Kawashima, R. A. Márquez, Y. J. Son, et al., "Accurate Potentials of Hg/HgO Electrodes: Practical Parameters for Reporting Alkaline Water Electrolysis Overpotentials," *ACS Catalysis* 13 (2023): 1893–1898.

71. J. N. Hausmann, B. Traynor, R. J. Myers, M. Driess, and P. W. Menezes, "The pH of Aqueous NaOH/KOH Solutions: A Critical and Non-Trivial Parameter for Electrocatalysis," *ACS Energy Letters* 6 (2021): 3567–3571.

Supporting Information

Additional supporting information can be found online in the Supporting Information section.

Supporting File: smll72688-sup-0001-SuppMat.docx.

Supporting File: smll72688-sup-0002-VideoS1.mp4.

Supporting File: smll72688-sup-0003-VideoS2.mp4.

Supporting File: smll72688-sup-0004-VideoS3.mp4.